Neuronal Excitability

Hetereogeneity in Neuronal Intrinsic Properties: A Possible Mechanism for Hub-Like Properties of the Rat Anterior Cingulate Cortex during Network Activity

Natalie E. Adams,[1,2,*] Jason S. Sherfey,[2,3,*] Nancy J. Kopell,[2] Miles A. Whittington,[4] and Fiona E.N. LeBeau[1]

[1]Institute of Neuroscience, Medical School, Newcastle University, Newcastle-upon-Tyne, NE2 4HH, UK, [2]Department of Mathematics and Statistics, Boston University, Boston, MA 02215, [3]Center for Computational Neuroscience and Neural Technology, Boston University, Boston, MA 02215, and [4]Department of Biology-F1, Hull York Medical School, York University, Heslington, YO10 5DD, UK

Abstract

The anterior cingulate cortex (ACC) is vital for a range of brain functions requiring cognitive control and has highly divergent inputs and outputs, thus manifesting as a hub in connectomic analyses. Studies show diverse functional interactions within the ACC are associated with network oscillations in the β (20–30 Hz) and γ (30-80 Hz) frequency range. Oscillations permit dynamic routing of information within cortex, a function that depends on bandpass filter–like behavior to selectively respond to specific inputs. However, a putative hub region such as ACC needs to be able to combine inputs from multiple sources rather than select a single input at the expense of others. To address this potential functional dichotomy, we modeled local ACC network dynamics in the rat in vitro. Modal peak oscillation frequencies in the β- and γ-frequency band corresponded to GABA$_A$ergic synaptic kinetics as seen in other regions; however, the intrinsic properties of ACC principal neurons were highly diverse. Computational modeling predicted that this neuronal response diversity broadened the bandwidth for filtering rhythmic inputs and supported combination—rather than selection—of different frequencies within the canonical γ and β electroencephalograph bands. These findings suggest that oscillating neuronal populations can support either response selection (routing) or combination, depending on the interplay between the kinetics of synaptic inhibition and the degree of heterogeneity of principal cell intrinsic conductances.

Key words: anterior cingulate; dynamic routing; intrinsic properties; modeling; network oscillations

Significance Statement

The anterior cingulate cortex (ACC) integrates diverse inputs and outputs to mediate higher cognitive functions. Experimental data demonstrated that fast network oscillations at both the β- and γ-frequency bands could be elicited *in vitro* in the rat ACC, and neurons exhibited a wide range of intrinsic properties. Computational modeling of the ACC network, constrained by the biological data, revealed that the frequency of network oscillation generated was dependent on the time course of inhibition. Neuronal response heterogeneity broadened the range of frequencies generated by the model network. In addition, with different frequency inputs to two neuronal assemblies, heterogeneity decreased competition and increased spike synchrony between the networks, thus conferring a combinatorial advantage to the network.

Introduction

Anterior cingulate cortex (ACC) is a functionally distinct area of the prefrontal cortex (PFC) that in rats, primates, and humans is associated with a broad range of functions, including remote spatial memory (Teixeira et al., 2006; Wartman et al., 2014), attention and executive function (Kesner and Churchwell, 2011; Newman et al., 2014), adaptive control (Narayanan et al., 2013), error detection (Ito et al., 2003; Hyman et al., 2013), and reward-based decision-making (Walton et al., 2003; Hillman and Bilkey, 2010). Such diversity of function, collectively referred to as cognitive control (Shenhav et al., 2013), supports the idea that the ACC may act as a general action-outcome predictor (Hyman et al., 2013).

A wide range of inputs to ACC suggest that, from a connectomic point of view, this region can potentially monitor all modalities of primary sensory input, affective state, motor state, and associational processing (Hoover and Vertes, 2007; Park and Friston, 2013; Vogt and Paxinos, 2014). Equally diverse outputs from ACC (Gabbott et al., 2005) would allow this area to function as a higher-order hub region, vital for multimodal integration (Bassett et al., 2008).

A dynamic view of brain connectivity reveals a rich variation in the interplay between one brain region and others that change over time scales of less than tens of milliseconds (Kopell et al., 2014). Functional connectivity, with quantifiable behavioral consequences, involves specific phase relationships between activity in different areas organized over a spectral range including β (20–30 Hz) and γ (30–80 Hz) frequency electroencephalograph (EEG) bands (Bastos et al., 2015). Within this frequency range, local neuronal networks can effectively select which inputs to respond to on the basis of the relative peak frequency of concurrent inputs—with faster frequencies taking precedence (Cannon et al., 2014). This selection of inputs can lead to routing of information based on the relative strength of the oscillations present in the inputs (Kopell et al., 2010; Akam and Kullmann, 2010, 2014).

Network oscillations in the β- and γ-frequency range in PFC subregions, including ACC, are associated with many cognitive functions (Buschman et al., 2012; Brincat

and Miller, 2015). This activity depends on local network interactions between excitatory principal cells and fast-spiking, parvalbumin-containing (PV) interneurons (e.g., Fisahn et al., 1998; Whittington et al., 2011). Computational studies have predicted that the input selection and routing behaviors of γ and β rhythms are, at least in part, manifested through the establishment of bandpass-filter behavior of local networks afforded by the kinetics of the synaptic inhibition provided by these PV neurons (Akam and Kullmann, 2010; Cannon et al., 2014). In contrast, it can be argued that the function of hub-like regions such as ACC should depend more on a combinatorial processing of inputs, with selection and routing processes more appropriate for regions critical for contextual disambiguation (Phillips et al., 2010).

Using in vitro recordings in rat ACC, we investigated the network properties of β- and γ-frequency oscillations generated locally and the diversity of intrinsic cellular properties of ACC principal cells. The data demonstrated that the generation of both β- and γ-frequency oscillations was critically dependent on the kinetics of fast synaptic inhibition, as widely reported in other brain regions (Whittington et al., 2011). Here we show that both passive and active intrinsic principal cell properties exhibited a great deal of heterogeneity. Computational studies, constrained by this biological data, showed that in response to rhythmic (sinusoidal) input, the kinetics of slow (13 ms) and fast (5 ms) synaptic inhibition decay times determined the center frequency of the bandpass-filtering properties of the ACC network to within either the β- or γ-frequency range, respectively. However, modeling the observed heterogeneity in the intrinsic properties of ACC neurons broadened the filter bandwidth at both β and γ frequencies. The main consequence of the broader filter bandwidths was to bias the local network behavior away from input selection and toward a more combinatorial behavior, consistent with the proposed hub-like function of ACC.

Methods

Slice preparation and solutions

Coronal slices (450 μm thick) containing the caudal regions of ACC (Cg1 and Cg2) were prepared from 2- to 3-month-old male Lister hooded rats. Rats were anesthetized with inhaled isoflurane, followed by an intramuscular injection of ketamine (100 mg/kg; Fort Dodge Animal Health) and xylazine (10 mg/kg; Animalcare). When all responses to noxious stimuli, such as pedal withdrawal reflex, had terminated, the animals were intracardially perfused with ~50 ml of modified artificial CSF (ACSF) composed of (in mM) 252 sucrose, 3.0 KCl, 1.25 NaH_2PO_4, 24 $NaHCO_3$, 2.0 $MgSO_4$, 2.0 $CaCl_2$, and 10 glucose. All procedures were in accordance with the UK Animals (Scientific Procedures) Act of 1986 and the European Union Directive 2010/63/EU.

After brain removal, 450-μm-thick coronal PFC slices were cut using a Leica VT1000S vibratome. Slices were then trimmed and transferred to a holding chamber at room temperature for ~1 h, which allowed washout of all anesthetic agents, before being transferred to a recording chamber, where they were maintained at ~29–31°C at

*N.E.A. and J.S.S. contributed equally to the work.

Correspondence should be addressed to F.E.N. LeBeau, Institute of Neuroscience, Newcastle University, Medical School, Framlington Place, NE2 4HH, UK. E-mail: fiona.lebeau@newcastle.ac.uk.

the interface between normal ACSF (where sucrose was replaced with 126 mM NaCl, and MgSO$_4$ and CaCl$_2$ were reduced to 1.2 and 1.76 mM, respectively) and humidified 95% O$_2$/5% CO$_2$. Drugs used were as follows: kainic acid (800 nM; Sigma-Aldrich); the AMPA/kainate receptor antagonist 2,3-dioxo-6-nitro-1,2,3,4-tetrahydrobenzo[f]quinoxaline-7-sulfonamide (NBQX; 10 μM); the NMDA receptor antagonist D-(-)-2-amino-5-phosphonopentanoic acid (D-AP5; 50 μM); and the GABA$_B$ receptor antagonist 3-aminopropyl-diethoxy-methyl-phosphinic acid CGP 35348 (5 μM).

Recording techniques

Extracellular recordings were performed with ACSF-filled glass microelectrodes (resistance <5 MΩ). Only one extracellular electrode was positioned in each slice, which was moved across the laminae until a clearly detectable oscillation was recorded. Intracellular recordings used glass microelectrodes (resistance 80–150 MΩ) filled with potassium acetate (2 M). To assess intrinsic membrane properties, ACC cells were recorded with antagonists of glutamatergic transmission including NBQX (10 μM), D-AP5 (50 μM), and CGP 35348 (5 μM) in the ACSF. Data were recorded via an Axoclamp amplifier (Molecular Devices), using an InstruTECH ITC-16 (HEKA Electronic, Digitimer) after live mains noise was removed using a Humbug (Quest Scientific, Digitimer) and preamplification and bandpass filtering between 1.5 and 300 Hz (Neurolog, Digitimer). Data were sampled at 5 kHz.

Data analysis

All time-series analyses were performed in MATLAB (MathWorks). Power spectra for all local field potential (LFP) and intracellular recordings were created using Welch's estimate on traces between 20 s and 1 min in length, using a window length of 5 s and a 50% window overlap. During postprocessing, the LFP data were processed up to only a frequency of 80 Hz.

Postsynaptic potentials

Inhibitory postsynaptic potentials (IPSPs) were recorded with cells held at a membrane potential of –30 mV (Fig. 1). IPSPs were analyzed using a custom-made Matlab script and were included only if the amplitude exceeded 0.5 mV. IPSP amplitude was calculated as the voltage difference between the trough of the IPSP and the preceding peak (start of the IPSP). Decay times of IPSPs were taken at 63% of the peak voltage deflection. Spike-triggered averaging was performed by taking the mean of all spiking events above a threshold of –40 mV with the spike peak forming the center of the average and including 50 ms before and 200 ms after the peak.

ACC cell intrinsic properties

Numerical values for intrinsic parameters (IPs) were collated for each cell (Fig. 2). The chosen IPs were as follows: IP1, action potential (AP) amplitude (mV); IP2, I_h (cAMP-dependent hyperpolarization-activated current) estimate (the amplitude of the sag potential from the steady state of –200 nA step injection and the subsequent return to rest; mV); IP3, afterhyperpolarization (AHP) am-

plitude (mV); IP4, AHP magnitude (voltage integrated over 200 ms post-AP; mV); IP5, AHP time to maximal deflection (ms); IP6, spike width at half-height (ms); IP7, spontaneous spike rate at threshold (Hz); IP8, resting membrane potential (rmp; mV); IP9, initial spike frequency (time between first and second spikes) on step depolarization (Hz); IP10, ratio of third to second interstimulus interval on step depolarization-induced spike train (used as a measure of spike frequency adaptation; unitless). After within-parameter normalization, the normalized cross-correlation coefficients between pairs of parameters were found. IPs that were correlated (or anti-correlated) above an absolute value of ±0.33 were considered significantly correlated and were discarded. The variance explained in the remaining IP dataset (IP3, IP5–IP10) was calculated for each property.

Cell clustering

Clustering was performed using *k*-means and hierarchical methods (Fig. 3). One-way ANOVA was used to compare parameter distributions across the clusters. After within-parameter normalization, the normalized cross-correlation coefficients between pairs of parameters were found, producing a correlation matrix of all pairs. Variables that were correlated (or anti-correlated) above an absolute value of ±0.33 were classed as significantly correlated variables and were discarded. Multivariate ANOVA analyses of the remaining parameters were performed on all pairs of clusters to determine whether cells could be clustered according to individual or combined parameters. Hierarchical clustering used Ward's minimum variance criterion. The effectiveness of clustering was tested for 2–10 clusters using the Davies–Bouldin index, which measures the ratio of intracluster scatter to intercluster separation, and Dunn's Index, which similarly assesses intracluster distance versus intercluster distance. Maximization of the Davies–Bouldin index and minimization of Dunn's Index provide internal measures of the effectiveness of the clustering (Davies and Bouldin, 1979; Maulik and Bandyopadhyay, 2002). Data were shuffled by reordering the values for each intrinsic property via a random permutation in Matlab.

Statistical analysis

Statistical analyses were performed in Sigmaplot 11.0 (Systat Software), and data are presented as median and 25%–75% interquartile range (IQR). Significance chosen was $p < 0.05$.

Computational modeling

Pyramidal cell model

We developed a single-compartment pyramidal cell model capable of producing the range of intrinsic membrane properties observed in ACC (Fig. 4). The conductance-based model had a membrane potential V (mV) governed by

$$C_m \frac{dV}{dt} = I_{inj}(t) - \sum I_{int} + \eta,$$

where t is time (ms), $C_m = 1$ μF/cm^2 is the membrane capacitance, $\eta = 0.01\varepsilon$ is Gaussian noise with $\varepsilon \sim N(0,1)$
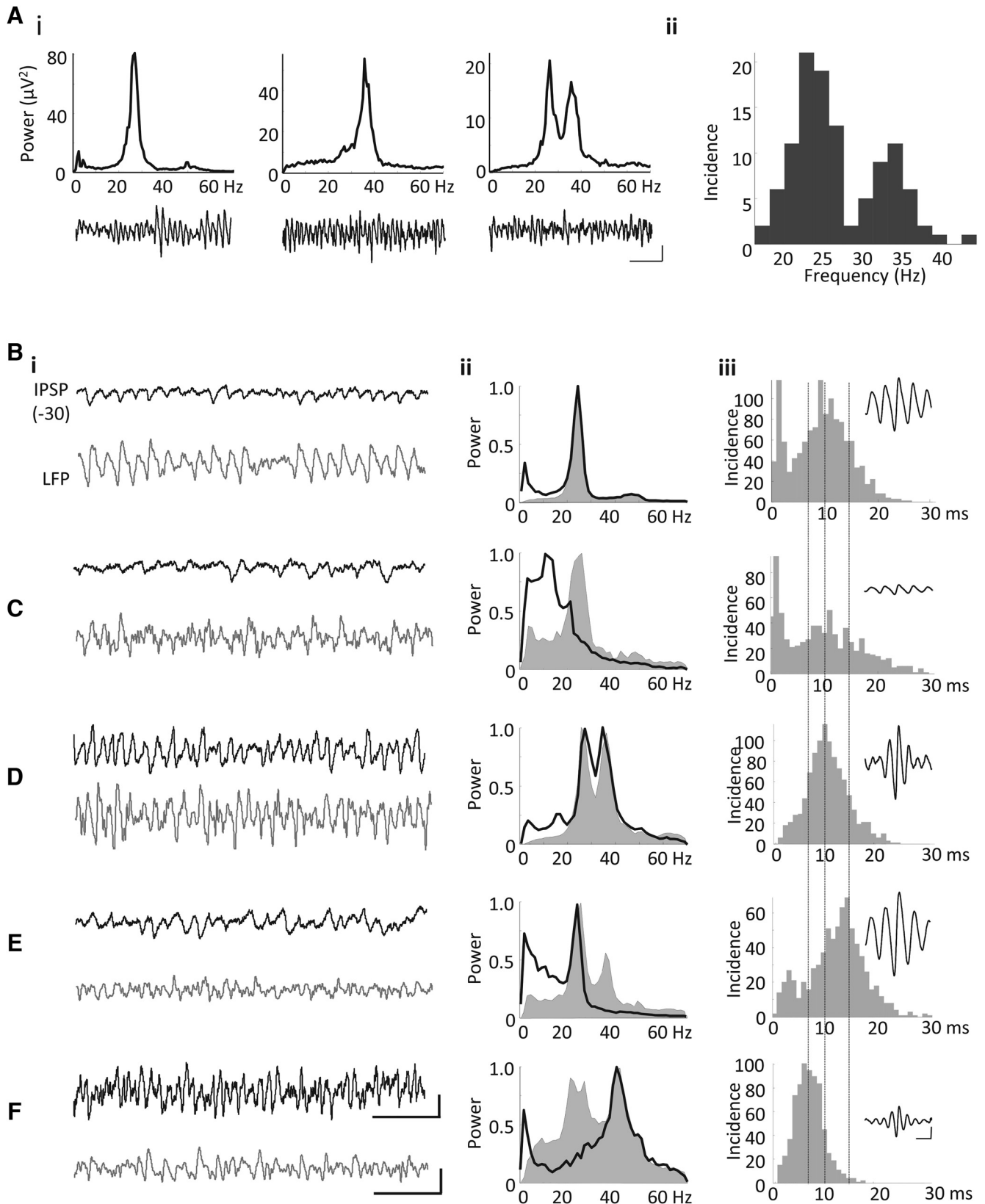
Figure 1. IPSPs suggest dual inhibitory inputs in ACC cells during γ/β network oscillations. **Ai**, Example power spectra and traces of KA-evoked oscillations showing representative local field potential oscillations from three different slices consisting of purely β rhythms (left), purely γ rhythms (middle), and a dual-frequency oscillation (right); scale bar 50 μV, 200 ms. **Aii**, Incidence plot for the modal peak frequencies in spectra from 109 ACC slices showing a clear bimodal average spectrum. **Bi**, **Bii**, Example IPSP traces

continued

(scale bar 5 mV, 200 ms) and simultaneously recorded LFP (scale bar 50 μV, 200 ms; ***i***) with corresponding normalized power spectra (***ii***) showing the LFP power spectrum (shaded) and overlaid IPSP power spectrum (black line). ***Biii***, Distribution of IPSP decay times. Inset shows IPSP-triggered averages of the LFP. ***B***, Field oscillation and IPSP at β frequency. ***C***, Field oscillations at β frequency but IPSPs at ~12 Hz. ***D***, Mixed γ/β frequency field oscillation and IPSPs. ***E***, Mixed γ/β field oscillations but IPSPs only at β frequency. ***F***, Mixed γ/β field oscillations but IPSPs only at γ frequency.

and amplitude tuned to match baseline fluctuations in membrane potential, $I_{inj}(t)$ is an injected current (μA/cm^2) simulating an *in vitro* experimental protocol, and I_{int} denotes intrinsic membrane currents (μA/cm^2) produced by ionic conductances with Hodgkin–Huxley-like channel kinetics from published cell models: I_{KDR}, I_{NaF}, I_{KS}, and I_{NaP} from Durstewitz and Seamans (2002) for spike generation and adaptation; I_{CaN}, I_{CaT}, I_{KCa}, and I_H from Papoutsi et al. (2013) for calcium-dependent adaptation, slow afterhyperpolarization, and hyperpolarization-induced voltage sag; and I_{AHP} from Yamada et al. (1998) (see legend of Fig. 4 for more details). Ionic currents from Durstewitz and Seamans (2002) and Papoutsi et al. (2013) were chosen because their kinetics were constrained by experimental data from rat medial PFC. Each active current was modeled as $I_{int} = g_{int}m^ph^q(V − E_{int})$, where maximal conductance g_{int} (mS/cm^2), reversal potential E_{int} (mV), p, q, and the kinetics of activation gate m and inactivation gate h were as published unless otherwise specified. All cells had a passive leak current $I_L = g_L(V − E_L)$ with conductance $g_L = 0.04$ mS/cm^2 and reversal potential E_L (mV).

The *in vitro* cell characterization experiment was simulated by a current injection, $I_{inj}(t)$, delivering a series of hyperpolarizing and depolarizing pulses, followed by a ramp to spike threshold, then constant depolarization (compare Fig. 4A). Model IPs were calculated from the simulated data using the same analysis applied to the experimental recordings. A set of cell models capturing the diversity observed in ACC was obtained by manually varying biophysical parameters and comparing model IPs to the aggregate (all cells, all layers) experimental distributions (Fig. 4C). Specifically, E_L and maximal values for eight active conductances (g_{KDR}, g_{NaF}, g_{KS}, g_{CaN}, g_{CaT}, g_{KCa}, g_H, g_{AHP}) were varied across simulations to find a set of models with IPs spanning the ACC distributions for the five most discriminative IPs from the experimental IP data analysis (IP5–IP9, accounting for 85% of the total variance in ACC IPs; see Fig. 4C). Parameter space was explored in two steps. First, each maximal conductance was logarithmically varied 1×10^{-6} to 1×10^2 to determine the scales over which realistic IPs could be observed. Next, hypercube subspaces were explored around the identified scales for maximal conductance and an E_L range spanning the recorded rmp values. Only parameter sets producing IPs within the experimental ranges were considered viable models of the pyramidal cells recorded *in vitro* in the presence of synaptic blockers. This procedure resulted in 2810 viable cell models of >100,000 simulated models.

All viable cell models had biophysical parameters yielding intrinsic electrophysiological properties within the ranges observed experimentally. Across the set of viable models, each biophysical parameter had a distribution of

values (Fig. 4C) and tended to covary with other biophysical parameters to some degree. We defined a homogeneous assembly of cells as a population of equivalent cell models with biophysical parameters set to medians computed across the full set of viable models; all cells belonging to a given assembly received similar inputs (see details below). Independent realizations of heterogeneous assemblies were generated by drawing biophysical parameters from a multivariate normal distribution using the covariance matrix, including all pairs of biophysical parameters, computed across the full set of 2810 viable models.

Biophysical network model

We developed a computational representation of a generic ACC network including single-compartment excitatory (E) pyramidal cells and inhibitory (I) interneurons. E-cells were modeled as previously described with the addition of synaptic inputs and exclusion of the injected current:

$$C_m\frac{dV}{dt} = -I_{ex}(t, V) − \sum I_{int} − \sum I_{syn} ,$$

where $I_{ex}(t,V)$ is an excitatory current (μA/cm^2) reflecting inputs from external sources and I_{syn} denotes synaptic currents (μA/cm^2) driven by other E- and I-cells in the network. I-cells were modeled using the fast-spiking (FS) Wang–Buzsáki interneuron model (Wang and Buzsáki, 1996). A more computationally demanding FS I-cell model based on PFC data (Durstewitz and Seamans, 2002) produced qualitatively similar results.

All networks consisted of 80 E-cells split into one or two assemblies coupled reciprocally to a shared pool of 20 I-cells (see model architecture in Figs. 5A, 5B, and 6A). E-cells provided excitation to all I-cells, mediated by α-amino-3-hydroxy-5-methyl-4-isoxazolepropionic acid (AMPA) currents. I-cells in turn provided inhibitory inputs γ-aminobutyric acid (GABA$_A$) currents to all E-cells and I-cells. AMPA currents were modeled as

$$I_{AMPA} = g_{AMPA}s(V − E_{AMPA}) ,$$

where V is the postsynaptic membrane voltage, g_{AMPA} is the maximal synaptic conductance, s is a synaptic gating variable, and $E_{AMPA} = 0$ mV is the synaptic reversal potential. Synaptic gating was modeled by

$$\frac{ds}{dt} = H(V_{pre})\frac{1 − s}{\tau_r} − \frac{s}{\tau_d} ,$$

where V_{pre} is the presynaptic membrane voltage, $\tau_r = 0.4$ ms and $\tau_d = 2$ ms are time constants for neurotransmitter release and decay, respectively, and $H(V) = 1 +$ tanh $(V/10)$ is a sigmoidal approximation to the Heaviside step function. GABA$_A$ currents are modeled in the same way
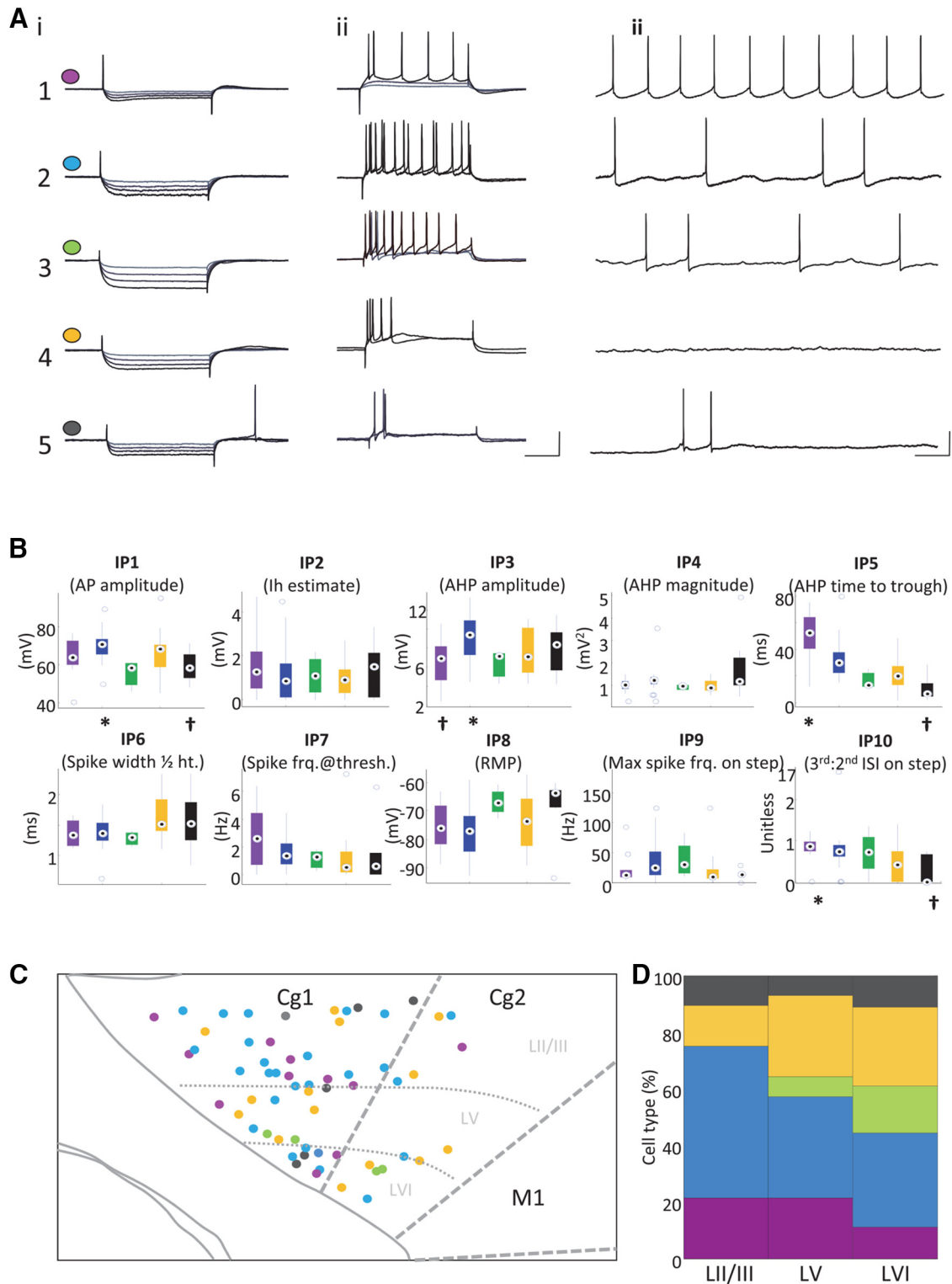
Figure 2. Manual classification and laminar distribution of cells in ACC. **A**, Each row shows the electrophysiological response properties of one example cell from groups 1–5: 400-ms hyperpolarizing steps at 0.1–0.4 nA (**i**); 400-ms depolarizing steps at 0.3–0.4 nA (**ii**; gray to black = smaller to larger current step; scale bar 20 mV, 100 ms). **Aiii**, Tonic activity at spike threshold (scale bar 20 mV, 200 ms). **B**, Values (medians and IQRs) for 10 IPs plotted for each manually selected group 1–5 (colors as in **A**). [†]Significantly different from * (one-way ANOVA, $p < 0.05$). Central circle, median values; blue circles, outliers. **C**, Schematic diagram of ACC (Cg1 and Cg2) with dots showing the location of cells found with different response properties. The color of each dot corresponds to cells from groups 1–5 recorded at each location. **D**, Plot shows the laminar distribution profile as a percentage of total cells in groups 1–5.
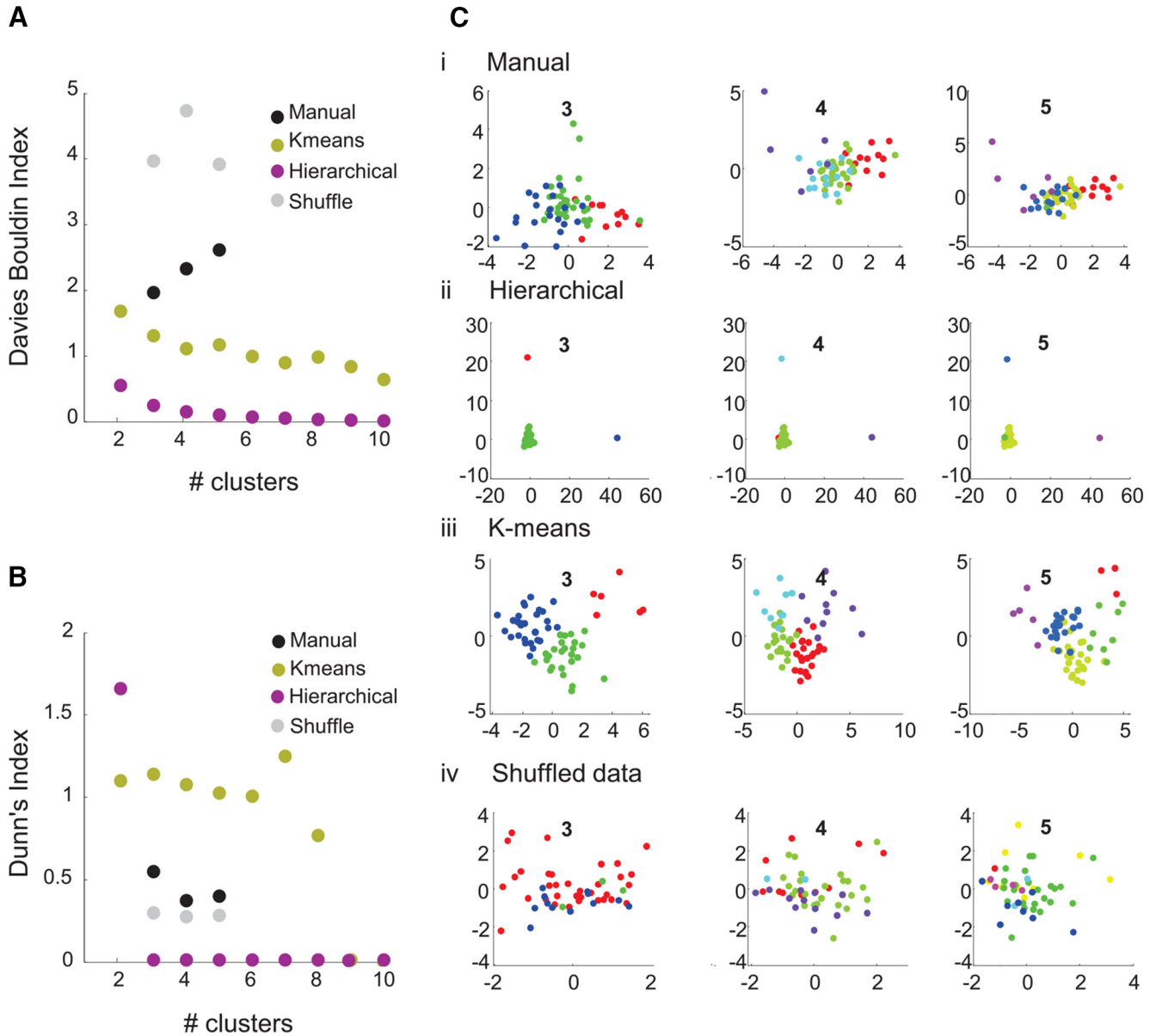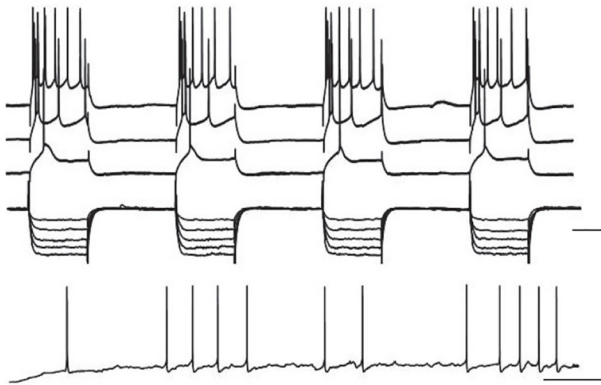
A

B

C

Figure 3. Objective clustering analysis does not identify distinct clusters. Validity indices Davies–Bouldin (**A**) and Dunn's (**B**) for the three clustering methods attempted; manual (black circles), k-means (olive circles), hierarchical (purple circles), and shuffled data (gray circles) for a range of cluster numbers (2–10 clusters). **C**, 2D canonical variable plots (unitless) from the multivariate analysis for the manual (**i**), hierarchical (**ii**), k-means (**iii**), and shuffled (**iv**) clusters when assuming three, four, and five clusters. Each plot shows the cells of each cluster as an arbitrary color.

with $E_{GABA} = -75$ mV and variable $\tau_d = \tau_I$ (5 or 13 ms, reflecting inhibition from different interneuron classes). Maximum synaptic conductances for E-cells, GABA$_A$ (0.1 mS/cm^2); for I-cells, AMPA (1 mS/cm^2) and GABA$_A$ (1 mS/cm^2).
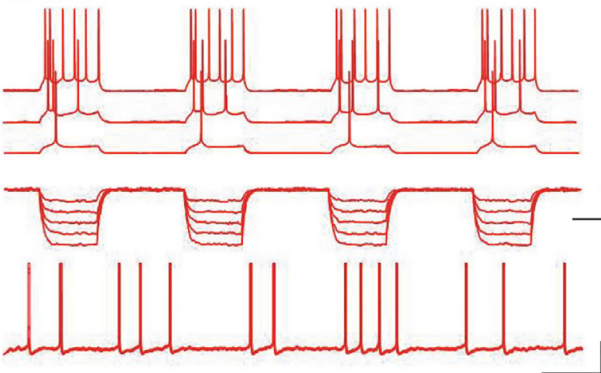
Excitatory/inhibitory (E/I) networks with one E-cell assembly were simulated to probe the natural and resonant frequencies of ACC networks with and without E-cell heterogeneity (Fig. 5). In these simulations, the input was a gated channel with excitatory AMPA current, $I_{ex} = g_{ex}s_{ex}(V - E_{ex})$, where E_{ex} is the synaptic reversal potential and s_{ex} is a postsynaptic gating variable that integrates independent Poisson spike trains with time-varying rate

function $\lambda(t)$. In different simulations, $\lambda(t)$ = (background activity) was used to probe natural frequencies $\lambda(t)$=r[1 + sin(2 πft)]/2 (rhythmic input) was used to probe resonant frequencies. Input spike trains represent background noise or rhythmic population activity originating from an arbitrary source network and are integrated in the synaptic gate s_{ex} with exponential AMPAergic decay. r was tuned during the former simulations to produce firing rates observed in the *in vitro* experiments with kainate-induced network oscillations. In the latter simulations, f was varied from 4 to 60 Hz (2-Hz steps) across simulations. All single-assembly simulations were repeated for $\tau_I = 5$ and 13 ms based on experimentally observed IPSPs in the γ- and
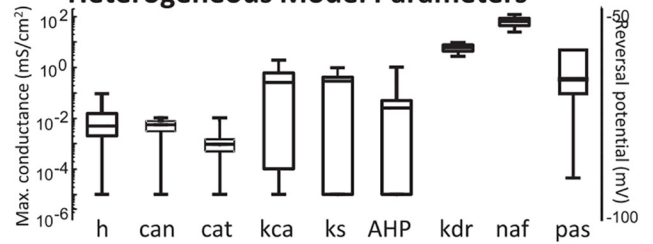
A Experiment

Model

B Heterogeneous Model Parameters

C Intrinsic Properties

AHP duration (IP5)

Spike width (IP6)

Spike frq. @ threshold (IP7)

RMP (IP8)
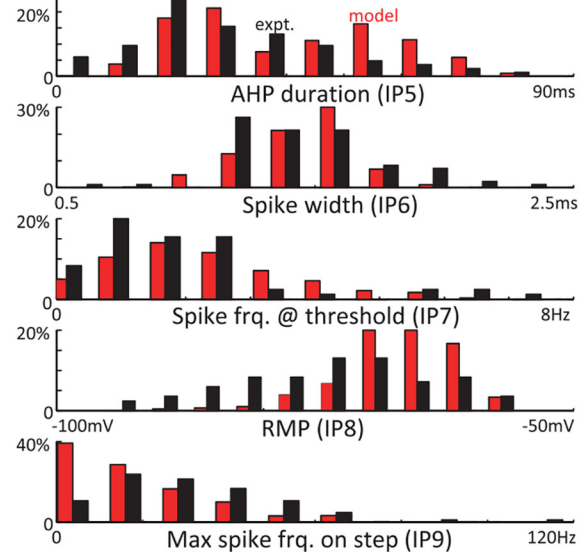
Max spike frq. on step (IP9)

Figure 4. Heterogeneous biophysical models reproduce the range of experimental intrinsic properties. **A**, Example of experiment and model cell responses to depolarizing current steps (top) and hyperpolarizing current steps (middle) and firing rate at rmp (bottom). Scale bars 20 mV/100 ms and 20 mV/2 s. **B**, Ion channel conductance ranges (10^{-6} to 10^2) used in ACC cell model. Values are based on model fits to experimental IP ranges. Ion channel key: h, HCN channel; can, high-threshold (N-type) calcium channel; cat, low-threshold (T-type) calcium channel; kca, calcium-dependent potassium channel; ks, slow (M-type) potassium channel; AHP, slow afterhyperpolarizing potassium channel; kdr, fast delayed rectifier potassium channel; naf, fast sodium channel; pas, passive leak channel. **C**, Model and experimental IP distributions for the 5 IPs (IP5–9) that explained most of the variance.

β-coherent cells, respectively. Parameters were set to $E_{ex} = 0$, $g_{ex} = 0.001$, and $r = 4500$ Hz.

E/I networks with two identical E-cell assemblies, E1 and E2, were simulated to probe the effects of heterogeneity on synchrony (integration) and competition between assemblies receiving noise or rhythmic inputs at different frequencies, f_1 and f_2, respectively (Fig. 6). In these simulations, the excitatory input was a gated AMPAergic response to a Poisson spike train as before. However, assemblies E1 and E2 received inputs from distinct source networks. Source network frequencies (f_1, f_2) were varied over a grid ranging from 7.5 to 60 Hz (7.5-Hz steps) across simulations, while the number of spikes delivered to each assembly was fixed. $\tau_I = 5$ ms and $\tau_I = 13$ ms were both used for the results reported below.

The diversity of cell intrinsic properties observed in ACC pyramidal cells was incorporated into heterogeneous E-cell assemblies as previously detailed. For a given simulation with two assemblies, the same cell models were used for both assemblies to ensure that differences in

their activities resulted from differences in their inputs and not differences in their cell properties.

All models were implemented in Matlab using the DynaSim toolbox (github.com/DynaSim) and are publicly available online at: github.com/jsherfey/ACd_model. Numerical integration was performed using a fourth-order Runge–Kutta method with a fixed time step of 0.01 ms. One- and two-assembly network simulations were run for 2000 and 5000 ms, respectively, and the first 500 ms was excluded from subsequent analysis. All network simulations were repeated 10 times.

Model analysis
Analysis of model networks with one assembly. The natural frequency of a network is the frequency of rhythmic population activity that emerges naturally given background activity. The natural frequency was identified as the frequency with peak power in Welch's spectrum of the mean E-cell voltage (simulated LFP) given an external input with constant g_{ex}. The resonant frequency of a network is the frequency of a rhythmic input for which the network exhibits maximal spiking. The resonant fre-
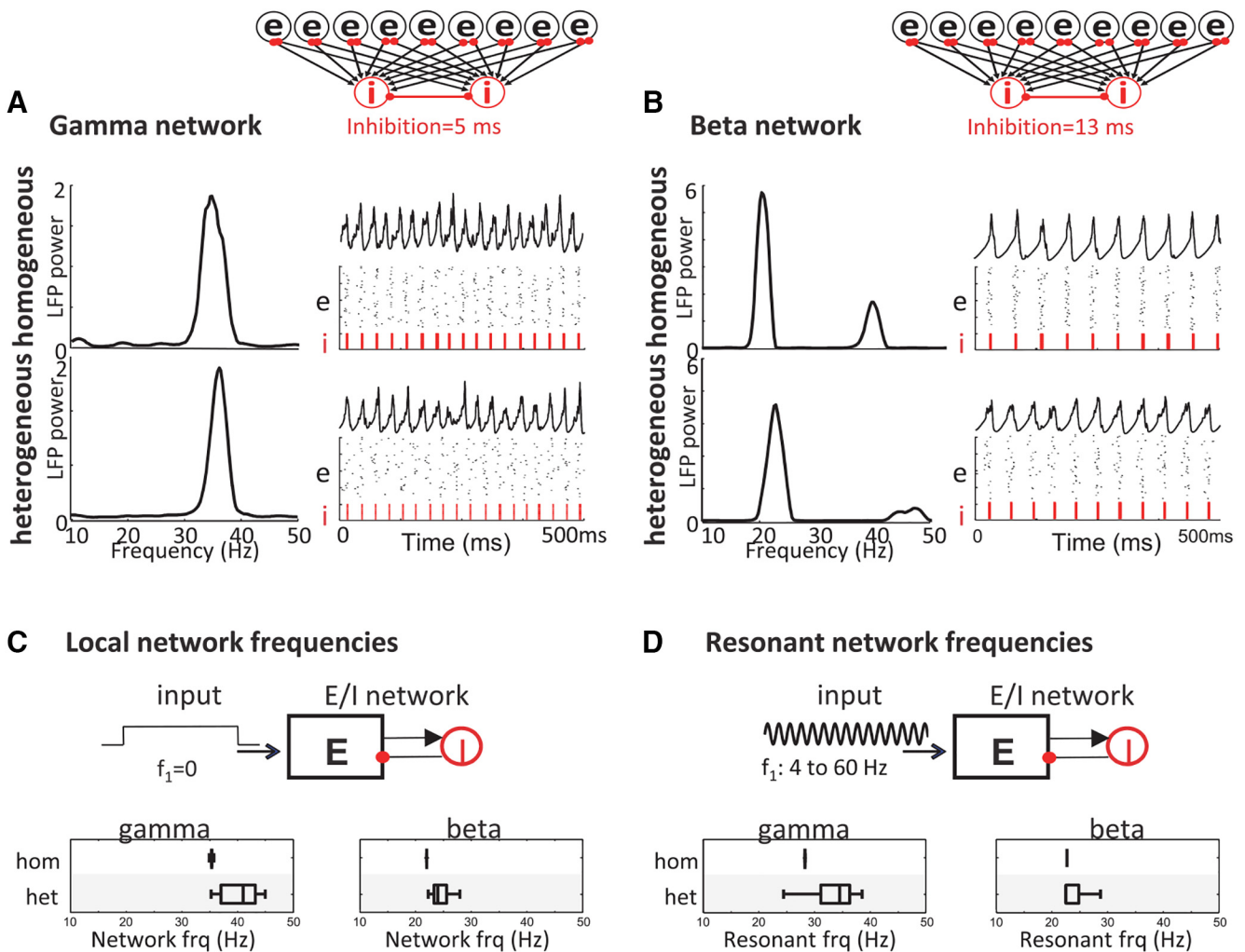
Figure 5. Cell diversity broadens intrinsic (local) oscillations and network tuning in ACC model. **A, B,** Network models were constructed by coupling the heterogeneous E-cell population to I-cells with time constants of inhibition based on the IPSP durations observed in cells rhythmic with the network β or γ rhythm in the LFP. The resulting E/I networks with fast (5 ms) and slow (13 ms) inhibition produced γ-frequency (**A**) and β-frequency (**B**) network oscillations whether the E-cell population had homogeneous or heterogeneous IPs. **C,** Effect of cell diversity on the intrinsic (local) frequency of network oscillations: Poisson noise input was applied to different 80-cell subsets of network E-cells on different realizations. Box plots show range of network frequencies for homogeneous and heterogeneous networks with different inhibition time constants at β and γ frequencies. **D,** Effect of cell diversity on network tuning (resonant frequency): a sinusoidal input was applied to different subsets of E-cells on different realizations, independently for each input frequency 4–60 Hz (in 2-Hz steps). Box plots show range of resonant frequencies of the homogeneous and heterogeneous networks.

quency was identified as the input frequency producing the maximum number of spikes in the E-cell assembly given an external input with sinusoidal g_{ex}.

Analysis of model networks with two assemblies. Two E-cell assemblies coupled to a shared pool of I-cells may differ in their amount of spiking (i.e., they may compete) or exhibit synchronous spiking to varying degrees (i.e., they may or may not support integration). The degree of competition between two assemblies, E1 and E2, was quantified by

$$\Delta = \frac{|N_1 - N_2|}{N_{max}},$$

where N_1 is the number of spikes in assembly E1, N_2 is the number of spikes in assembly E2, and N_{max} is the number of

spikes in the more active assembly. Δ indicates how much more active a dominant assembly is compared with a less active assembly; it varies between 0 (equal activity levels) and 1 (total suppression of the nondominant assembly). The degree of spike synchrony between two assemblies was quantified using the percentage of 10-ms time bins for which spiking occurred in both assemblies. Competition and synchrony were compared between homogeneous and heterogeneous networks using a two-sample *t* test and were considered significant if $p < 0.05$.

Results

Kainate-evoked network oscillations in ACC

Glutamatergic excitation via bath application of the kainate receptor agonist kainic acid (KA; 800 nM) was the
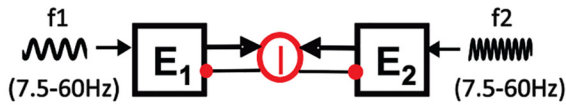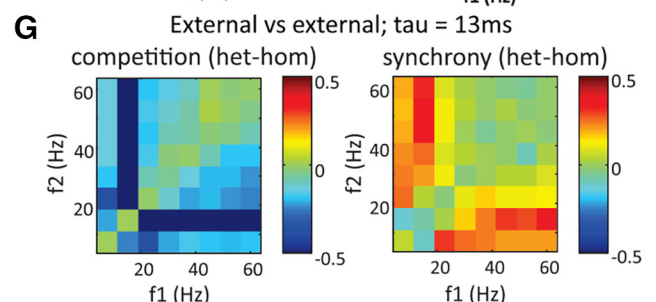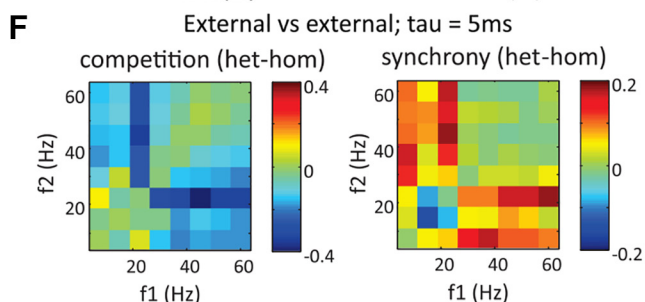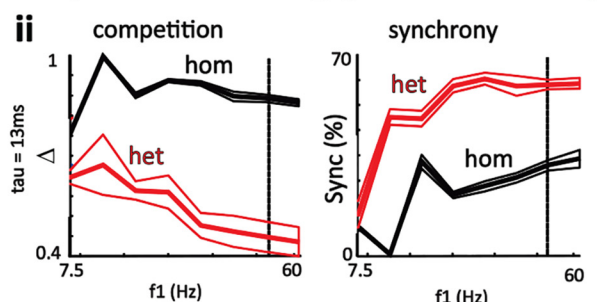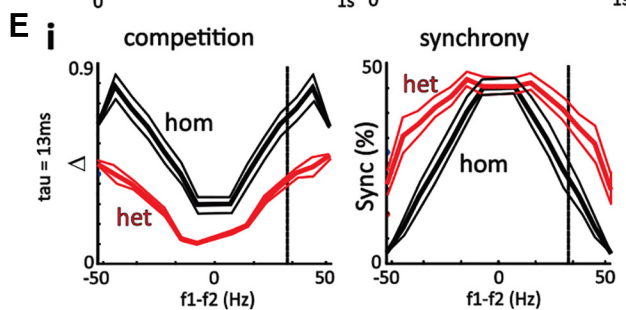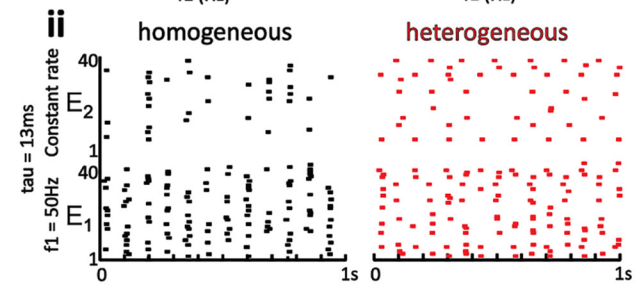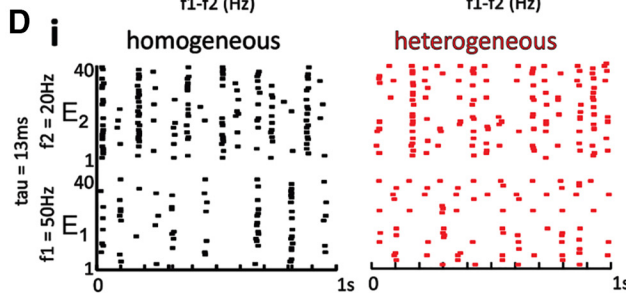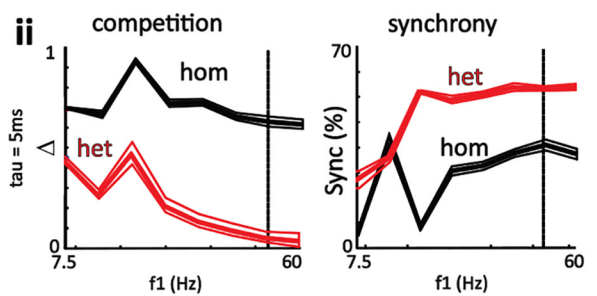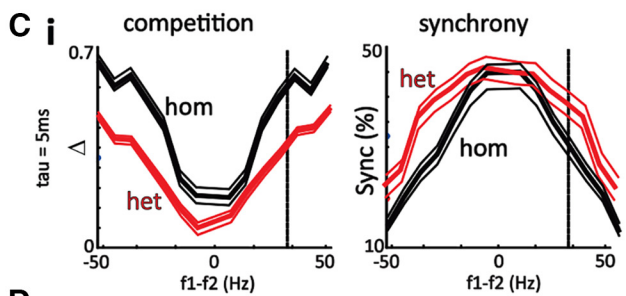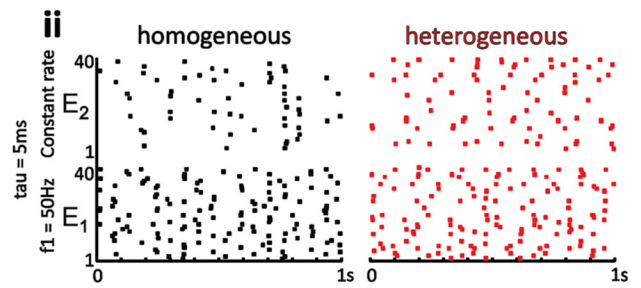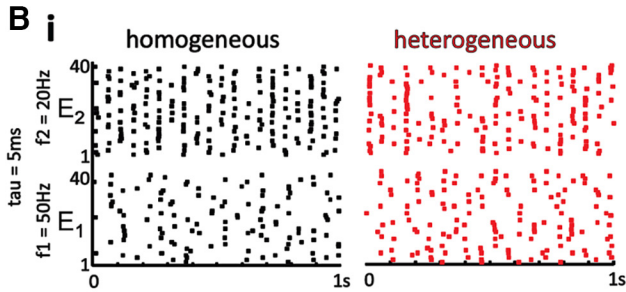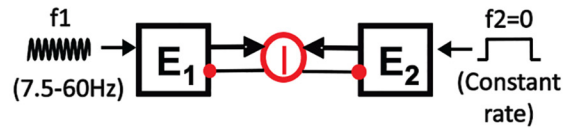
Figure 6. Heterogeneity increases synchrony and decreases competition between cell assemblies. *Ai*, Model schematic showing two excitatory assemblies, E1 and E2, receiving rhythmic AMPAergic inputs with equal spike counts and time-varying Poisson rates

continued

modulated at frequencies f_1 and f_2, respectively. The assemblies compete through a shared pool of inhibitory interneurons (I-cells), and $\tau_I = 5$ ms and $\tau_I = 13$ ms were used for these results. ***Bi***, For homogeneous assemblies (left) driven by external rhythms, the assembly with a more resonant input (e.g., 20 Hz) suppresses spiking in the assembly driven by a less resonant input (e.g., 50 Hz). Heterogeneity of cell intrinsic properties decreases this competition (right) and increases synchrony between the two assemblies (i.e., the fraction of 10-ms bins with spiking in both E1 and E2). ***Ci***, Heterogeneity decreases competition (Δ) across all pairs of input frequencies and increases synchrony for inputs separated by >30 Hz. Solid lines represent the $f_1 - f_2$ shown in the above raster plots. ***Di***, ***Ei***, Similar raster plots and plots of competition and synchrony for $\tau_I = 13$ ms. Again, heterogeneity decreases competition across all pairs of input frequencies and increases synchrony for inputs separated by >30 Hz. ***Aii***, Model schematic showing two assemblies, E1 and E2, receiving external rhythmic and background noise inputs, respectively, with the latter driving a local rhythm at the natural frequency of E2 (as in Fig. 5A). ***Bii***, The less resonant input from ***Bi*** strongly suppresses an assembly driven by a nonrhythmic Poisson input with equal spike count and constant rate. Heterogeneity decreases competition and increases synchrony. ***Cii***, Heterogeneity again decreases competition for all input frequencies and increases synchrony for frequencies >20 Hz. ***Dii***, ***Eii***, Similar raster plots and plots of competition and synchrony for $\tau_I = 13$ ms; again, heterogeneity decreases competition and increases synchrony in a very similar manner to $\tau_I = 5$ ms. Solid lines represent the f_1 shown in the above raster plots. ***F***, Plots show differences (heterogeneous – homogeneous) in mean competition and synchrony for $\tau = 5$ ms plotted as f_1 against f_2 on separate axes. ***G***, Same as ***F*** except $\tau = 13$ ms.

sole pharmacological manipulation necessary to produce a range of network oscillatory activity. Example power spectra with the associated LFP traces from three different experiments showed that the ACC oscillations could consist of either a single peak at β frequencies ($n = 81/109$; 74%), a single peak at γ frequencies ($n = 16/109$; 15%), or dual peaks at both β and γ frequencies ($n = 12/109$; 11%), (Fig. 1*Ai*). Oscillations at γ and β frequency could be observed in both deep and superficial layers. LFP recordings from all layers of ACC were combined, and the frequency of the oscillation evoked varied from 18 to 44 Hz ($n = 109$ slices) but resulted in a bimodal distribution with peaks at β frequencies (~24 Hz) and γ frequencies (~34 Hz; Fig. 1*Aii*).

Local network inhibition

IPSPs were recorded during KA-evoked field oscillations from morphologically unidentified cells in ACC ($n = 10$), and a variety of different IPSP properties were observed. When a β-frequency oscillation was recorded in the LFP, the IPSPs recorded intracellularly were either rhythmic with the recorded LFP (Fig. 1*Bi*) or nonrhythmic with the concurrently recorded LFP (Fig. 1*Ci*). If the IPSPs were nonrhythmic at the LFP frequency (Fig. 1*Ci*), they still exhibited rhythmicity, but with a peak power below ~12 Hz. When dual β-γ oscillations were recorded in the LFP, the IPSPs were either rhythmic at both frequencies (Fig. 1*Di*) or at only β (Fig. 1*Ei*) or γ (Fig. 1*Fi*) frequency.

The decay times for the IPSPs that were rhythmic with the β-frequency field oscillation were slower (modal peak 15 ± 3.5 ms; Fig. 1*Bi*) than IPSPs found to be rhythmic with the γ-frequency field oscillation (modal peak 6 ± 1.8 ms; Fig. 1*Fi*). In total, 8 of 10 cells were rhythmic with the field at either β or γ frequency. Overall, the results demonstrated that network inhibitory inputs mostly correlated with the bimodal nature of peak spectral frequencies seen in local field potentials such that IPSPs were largely either at β or γ frequency only. A correlation between field and IPSP frequency has been reported many times for network oscillations in primary sensory and polymodal association areas, reflecting the critical role of synaptic inhibition in shaping fast network dynamics (Whittington et al., 2011).

The above results revealed nothing unique in the profile of synaptic inhibition in ACC that could reflect the proposed hub-specific dynamic behavior that we predicted should be present in this region. We therefore switched our attention to examining the intrinsic principal neuronal properties that are known to be diverse in both rat (Yang et al., 1996; van Aerde and Feldmeyer, 2015) and primate (Ardid et al., 2015) PFC.

ACC intrinsic cell properties

We recorded from 61 cells in the ACC in the presence of excitatory transmitter blockers (see Methods) and found a wide variety of IPs, as has been previously reported in the prelimbic and infralimbic regions of the PFC (Yang et al., 1996; Dembrow et al., 2010; Gee et al., 2012; van Aerde and Feldmeyer, 2015; Glykos et al., 2015).

Initially, cells were characterized manually by segregating cells according to their AHP shape and firing characteristics from step and tonic depolarizations. Fig. 2*A* illustrates the variety of electrophysiological characteristics, organized into manually created categories (groups 1–5). The presence of a distinct fast AHP was evident in some cells, either with or without an afterdepolarization (ADP) potential. Tonic injected current at the threshold for spiking showed that some cells fired continually, whereas others fired less frequently, with a low frequency intrinsic subthreshold oscillation (ISO) evident between spikes. Other cells did not fire at all on depolarization or required rapid acceleration of depolarizing current to produce any spikes. Some cells had very little spike accommodation, whereas others had very fast adapting properties. The five manually classified groups were defined as follows (Fig. 2*A*): group 1 (11 of 61, 18% of cells) had an AHP duration (~200 ms), usually with a small ADP, little spike adaptation, and a spiking frequency of ~5 Hz at threshold. Group 2 (27 of 61, 44% of cells) had similar properties to group 1 with respect to spike adaptation, but the AHP had a more variable duration (~100–500 ms), and firing rates at threshold were less regular. Group 3 (3 of 61, 5% of cells) had a sharp AHP, clear spike adaptation, and irregular firing rates at threshold. Group 4 (14 of 61, 23% of cells) had very strong spike adaptation, rounded, short AHPs, and little or no firing after the initial spikes at

threshold. Group 5 (6 of 61, 10% of cells) always had a characteristic fast AHP, interrupted by an ADP, then a long AHP, and exhibited strong spike adaptation. Without morphologically identifying cells, we could not determine whether any of these groups corresponded to classes of interneurons, rather than putative pyramidal cells, but no distinct fast-spiking (FS) interneurons were recorded in this study.

In all cells, we measured 10 intrinsic properties (IP1–10; Fig. 2B) as described in Materials and Methods. Each of these IPs reflects the presence and magnitude of intrinsic conductances that are known to influence neuronal resonance (input-filtering) properties (see Discussion). The IPs of all cells were compared across each of the manually selected groups (groups 1–5), but very few significant differences were found, and those that were identified did not show any obvious pattern (Fig. 2B). In addition, the distribution of cells in group 1–5 across the laminar structure of ACC was diffuse, as most cell types could be found in all layers (Fig. 2C, D). These data demonstrate that in the ACC, different cell classes could not be defined by either a unique expression of ion channel properties or laminar position.

To assess whether ACC cells could be separated into discrete clusters, both hierarchical and k-means clustering were used in an attempt to segregate the cells, assuming 2 to 10 clusters. The Davies–Bouldin index and Dunn's index for a range of clusters from 2 to 10 for all clustering methods used in this study are plotted (Fig. 3A, B). In the Davies–Bouldin plot (Fig. 3A), the lower the index value, the better the cluster separation. Using Dunn's Index (Fig. 3B), the higher the index value, the better the cluster separation. k-means performed the best overall at various cluster sizes, followed by manual clustering; shuffled data gave the worst performance. The hierarchical cluster analysis performed best at the two-cluster level, but other values on, or close to, the zero line suggest that this analysis failed at higher cluster numbers. However, although these data show that our manually selected clusters performed better than the shuffled data, the clusters were still not clearly separated by any method used here. All clustering of cells found using the different methods are shown for three, four, and five assumed clusters on 2D plots (Fig. 3C) of the first two canonical variables from the MANOVA analysis. For k-means clustering, at the three-cluster level (Fig. 3Ciii, left), all three clusters were significantly different from each other in the first canonical variable dimension (x-axis; $p < 0.05$). However, although the k-means method performed optimally of the chosen methods in terms of the validity tests (Dunn's and Davies–Bouldin) as described above, two of the clusters (green and blue) can be seen to lie along a continuum, with no clear space separating them. In addition, relating these clusters individually back to the original electrophysiological characteristics yielded few significant differences, as with the manually selected clusters. At the three-cluster level using k-means, one cluster was separable ($p < 0.05$) in terms of spike rate at threshold, and one other cluster was separable ($p < 0.05$) in terms of resting membrane potential.

Biophysical diversity reproduces IP diversity in computational cell models

The above analyses strongly suggested a broad continuum of intrinsic ACC principal cell properties. To understand how such a situation may influence local network behavior, we first modeled this diversity computationally. A set of biophysical computational ACC cell models was generated to capture the above spread of IP values. Cells in this model could reproduce the firing properties of cells observed experimentally (Fig. 4A). A range of ion channel conductances was identified for each of eight different ion channels that reproduced the distribution of IP values recorded experimentally (Fig. 4B). Notably, this method did not explicitly constrain IP distribution shapes, yet the simulated IPs distributed similarly to the experimental IPs in most cases (Fig. 4C). Five IPs explained >85% of the total variance in the experimental data (IP5, AHP duration; IP6, spike width; IP7, spike rate at threshold; IP8, resting membrane potential; and IP9, instantaneous spike frequency) and were included in the model. In addition, we compared the correlations between z-scored IP values recorded in each cell with those from all model cells. This analysis showed that each experimental cell had at least one model cell with a value of $R^2 > 0.85$, and 90% of experimental cells had at least one model cell with $R^2 > 0.9$, indicating a very high correlation between the experimental and modeled IP values.

β and γ frequency rhythms were generated by different inhibitory decay constants in an ACC network model

To predict a possible role for the observed heterogeneity of IPs, the range of E-cells modeled above were combined with local circuit interneurons and inserted into an ACC network model (Fig. 5). Results from this model were compared with a model containing homogenous E-cell populations in which the intrinsic properties were the same for all cells in the population (see Materials and Methods). Heterogeneity was based on model parameters drawn from a multivariate distribution that preserves the correlation between the biophysical parameters producing cell responses constrained by experimental IPs (see Materials and Methods)

The different β and γ frequencies observed experimentally could be replicated in both the heterogeneous and homogeneous E-cell–containing models by switching the interneuron population inhibitory decay time constant (τ) from 5 to 13 ms (Fig. 5), consistent with experimentally observed values (see above). Simulation of all the heterogeneous E-cell models resulted in a broad distribution of oscillation frequencies, predominantly within either the β- or γ-frequency band, depending on the set inhibitory decay time constant (Fig. 5). This effect was similar regardless of whether the E/I assembly was driven by background activity (Poisson noise) or a rhythmic input. In both cases, cell diversity broadened the range of frequencies generated by the networks, but with different inhibition time constants resulting in largely separable frequency ranges at β and γ frequency (Fig. 5C, D).

Network heterogeneity decreases competition and increases synchrony among multiple assemblies

The above simulations led us to hypothesize that the experimentally observed heterogeneity in ACC might confer a computational advantage to a region that may have to combine multiple inputs at different peak frequencies within a given EEG band. To compare the effects of two different inputs on both the homogeneous and heterogeneous E-cell networks, we ran simulations with two E-cell assemblies connected to the same I-cells both receiving external rhythmic inputs (Fig. 6A). With this model configuration, we then assessed whether heterogeneity of cell properties in the model altered the network's response to multiple different inputs. Competition and synchrony were compared between the networks with homogeneous and heterogeneous E-cell assemblies with a shared pool of inhibitory interneurons (I-cells) and $\tau_I = 5$ and 13 ms (Fig. 6A–Ei). Fig. 6B shows example raster plots for two assemblies driven by rhythmic inputs at 20 and 50 Hz. In the homogeneous network, assembly E2, driven by an input at 20 Hz, dominated overall activity, although assembly E1 was being driven by an input with faster 50-Hz modulation across the population. When spiking occurred in the less active assembly (E1), it had a moderate degree of synchrony with the dominant assembly (E2). In contrast, in the heterogeneous network, receiving the same 20- and 50-Hz inputs, both assemblies were now able to sustain more equal activity levels throughout the simulation, and with a greater degree of overlap in spike timing. Very similar results were obtained with interneuron population inhibitory decay time constants at both $\tau_I = 5$ ms and $\tau_I = 13$ ms. These examples emphasize how a wider diversity of cell properties within assemblies can increase the spike synchrony and decrease competition among multiple assemblies. Over a range of input frequencies f_1 and f_2, the degrees of competition and synchrony between target assemblies E1 and E2 were related to the proximity of their input frequencies. Competition in the heterogeneous network was reduced across all values of f_1 and f_2. Furthermore, for assemblies driven by inputs separated by >30 Hz (i.e., across EEG β- and γ-frequency bands), heterogeneity significantly increased spike synchrony.

Similarly, in separate simulations where only one cell assembly (E1) received an external rhythmic input and the other assembly (E2) received an equal-rate Poisson noise, the degree of competition and synchrony between target assemblies E1 and E2 were related to the frequency f_1 of the external rhythm (Fig. 6A–Eii). However, in this condition the interaction involved E1 following an external rhythm and E2 exhibiting a noise-driven local rhythm at its natural frequency (as in Fig. 5A). Given this interaction between external and local rhythms, heterogeneity reduced competition across all values of f_1 to a greater extent than occurred for two assemblies driven by external rhythms. Furthermore, a wider diversity of cell properties increased spike synchrony between externally driven and locally generated rhythmic assemblies to a greater extent for β and γ rhythmic inputs. Again, very similar results were obtained with interneuron population inhibitory decay time constants at both $\tau_I = 5$ ms and $\tau_I =$

13 ms (Fig. 6A–Eii). Replotting the data as f_1 versus f_2 along separate axes for both $\tau_I = 5$ ms and $\tau_I = 13$ ms shows the largest reduction in competition and increase in synchrony within the β- and γ-frequency bands (Fig. 6F, G).

Discussion

The present findings support the evidence that ACC generates γ- and β-frequency oscillations as a consequence of local circuit interactions between principal cells and interneurons. This type of local circuit behavior is near-ubiquitous in cortex (Whittington et al., 2011). The generation of β- and γ-frequency activity does not, alone, therefore present any clues as to the proposed hub-like role of ACC in combining multiple inputs required for its general role in cognitive control (Lapish et al., 2008; Durstewitz et al., 2010; Shenhav et al., 2013; Ma et al., 2014). However, in ACC, we found that this fundamental, inhibition-based mechanism of rhythm generation was present, along with considerable heterogeneity of principal cell intrinsic properties. Computational modeling predicted that an inhibition-based oscillation, combined with such heterogeneity, would have a limited effect on the locally generated rhythm, but a potent effect on the network's response to diverse oscillatory inputs. Neuronal response heterogeneity caused a transition from a network behavior, in which frequency-selected single inputs generated a single local ACC network output, to a combinatorial behavior, in which the network could combine oscillating inputs of different frequency.

Local generation of γ and β oscillations

We have demonstrated that γ- and β-frequency oscillations can be evoked in the ACC in vitro with application of KA alone. This is consistent with data in vitro from the hippocampus (Hájos et al., 2000; Hormuzdi et al., 2001; Fisahn, 2005) and neocortex (Roopun et al., 2008a; Anver et al., 2011; Ainsworth et al., 2012), where KA application has also been shown to evoke fast network oscillations in the 20- to 80-Hz frequency range. Network oscillations in the β- and γ-frequency range in ACC are dependent on GABA$_A$ and AMPA receptors (Steullet et al., 2014). With the exception of β rhythms in parietal association areas (Roopun et al., 2006), this pharmacological profile is consistent with other local cortical γ and β oscillations that are an emergent property of the network and reflect the activation by KA of a reciprocally connected pyramidal-fast spiking interneuron network (Whittington et al., 2011).

The distinction between γ- and β-frequency oscillations corresponded to the presence of IPSPs with different decay kinetics recorded from morphologically unidentified cells in ACC. The IPSP values obtained were consistent with the kinetics of GABA$_A$ receptor–mediated events associated with γ oscillations in hippocampus and neocortex and β oscillations in auditory cortex (Whittington et al., 1995; Ainsworth et al., 2011). The most parsimonious explanation for these two different frequencies of network activity, and two different inhibitory decay times, would be that distinct interneuron subtypes differentially contributed to the β- and γ-frequency oscillations (Roopun et al., 2008a). PV- and somatostatin-expressing interneu-

rons in the PFC have been shown to contribute to distinct behavioral functions (Kvitsiani et al., 2013; Pinto and Dan, 2015). Such interneuron subtype–specific functions might therefore correlate with the distinct network activities at β and γ frequencies. β-frequency oscillations have been proposed to play a role in establishing functional long-range connections, whereas γ-frequency oscillations are thought to be more important for local interactions (Donner and Siegel, 2011; Kopell et al., 2010). In addition, γ-frequency activity may mediate feed-forward interactions, whereas β-frequency activity has been proposed to mediate feed-back interactions (Bastos et al., 2012, 2015; but see below).

Variability of oscillatory inputs to ACC

A principal underlying the role of oscillations in determining functional connectivity between brain areas is that, within a classic EEG frequency band, they provide a mechanism by which neurons generate outputs at times appropriate for optimizing their mutual influence (Ainsworth et al., 2012). For this so-called communication through coherence to occur, matching the phase and frequency of oscillations in the connected areas is important (Fries, 2005). However, even within a classic EEG band, the network oscillation frequencies can vary enormously. In the case of γ oscillations, frequency can vary as much as 20 Hz depending on the region of origin (Middleton et al., 2008; Herrmann et al., 2010) and the properties of the sensory input that generates them (Orekhova et al., 2015; Perry et al., 2015). Similarly, β oscillations in different brain regions may vary in peak frequency by up to 10 Hz (e.g., van Burik et al., 1998; Roopun et al., 2008b).

Within brain regions receiving concurrent oscillating inputs in the γ or β EEG bands, even subtle frequency differences have been predicted to have dramatic effects. In networks where the dominant time-constant governing rhythmicity is that of synaptic inhibition, one input at a slightly faster frequency than another can effectively abolish any influence the slower frequency has on local spike generation (Cannon et al., 2014). Similarly, synchronous inputs can be readily separated from asynchronous inputs (Akam and Kullmann, 2010), but if multiple inputs arrive at similar frequencies they can become mutually distracting (Akam and Kullmann, 2014). Therefore, if a local network such as the ACC is to combine multiple oscillating inputs, a network property additional to the rhythmicity afforded by local inhibition must be present. Data and computational modeling presented here strongly suggest that heterogeneity in intrinsic neuronal electrophysiological properties may provide such a combinatorial advantage to the network.

Intrinsic electrophysiological properties of neurons in ACC

Neurons recorded in this study could be subjectively divided into five broad groups similar to those described in other PFC regions (Yang et al., 1996; Dembrow et al., 2010; Gee et al., 2012; Lee et al., 2014; Glykos et al., 2015; van Aerde and Feldmeyer, 2015). However, using a range of established clustering algorithms that have been used successfully in other cortical areas to identify distinct neuronal clusters based on electrophysiological properties (Sosulina et al., 2006; Keshavarzi et al., 2014; Ferrante et al., 2016), we did not identify distinct clusters. Three significantly different clusters could be distinguished using k-means clustering, but the clusters were not well separated and they could not be replicated using hierarchical clustering. Our data, therefore, suggest a broad continuum of electrophysiological properties present in ACC neurons, with this heterogeneity mediated by the relative density of intrinsic conductances, including passive and voltage-gated potassium channels, persistent sodium channels, and HCN channels. These channels have overt effects on intrinsic neuronal properties (He et al., 2014) and are vital for controlling the resonance and thus dynamic input-filtering properties of neurons (Hutcheon and Yarom, 2000). In turn, bandpass input filtering is vital for input selection and routing of oscillatory inputs (Kopell et al., 2010; Akam and Kullmann, 2010, 2014).

Neocortical areas can also exhibit considerable heterogeneity in electrophysiological properties as evidenced by the recent extensive documentation of neuronal circuits within the somatosensory cortex (Markram et al., 2015). As discussed by Markram et al. (2015), in addition to intrinsic properties, there can also be heterogeneity of synaptic properties such as decay times, synaptic depression, and facilitation, which can vary between cell types (Thomson et al., 1996). However, Markram et al. (2015) describe electrically stimulated and spontaneous activity in the neocortex, and not the properties of neurons during an emergent network rhythm, such as β- and γ-frequency activity. Our data demonstrate that there is little variability in, for example, decay times of the IPSPs that correlated with either the β- or γ-frequency field oscillation.

One interesting feature we observed was the lack of any clear laminar segregation in the generation of either β- or γ-frequency activity within the ACC. This is in marked contrast to other neocortical areas where several studies in vitro have shown that γ-frequency activity is generated in the superficial layers (II/III), whereas β-frequency activity arises from deep (V/VI) layers (Roopun et al., 2008a; Ainsworth et al., 2012). No such obvious laminar distinction was seen in this study, and both β- and γ-frequency activity could be recorded from all layers. This difference in organization may reflect the absence of a functional layer IV in ACC, or may in fact reflect the integrative function of ACC, such that oscillations of different frequencies occur across all the laminae.

Consequences for ACC functionality in a dynamic network

The data and model presented here suggested that the modal peak frequency of an oscillation in ACC was predominantly governed by the time course of synaptic inhibition. This was the case both when the observed diversity of intrinsic properties was used and when principal neuron properties were homogeneous. The biggest difference made by the observed intrinsic heterogeneity was a broadening of the input-filtering characteristics of the model ACC network and a resulting ability of the

network to respond to multiple inputs of differing frequencies concurrently within either the γ or β EEG bands. This is consistent with the ideas of Seamans and colleagues (Lapish et al., 2008; Durstewitz et al., 2010; Ma et al., 2014), who consider ACC as consisting of "overlapping cell assemblies encoding various cognitive events involved in a decision-making process." The emergence of a broader range of local and resonant frequencies, afforded by cellular diversity, would promote diverse inputs to equally influence the same target (ACC).

Interestingly, with the degree of model heterogeneity constrained by the biological data gathered, the broadening of input filter characteristics predicted a decrease in competition and increased synchrony between ACC regions receiving or generating both γ and β frequencies. This seems antagonistic to proposed functions of discrete frequency bands such as hierarchical organization of signals (Lakatos et al., 2005), concatenation (Roopun et al., 2008b), and segregation of top-down and bottom-up signals (Bastos et al., 2015). However, with ACC sitting at the top of the functional connectivity hierarchy in the cortex, these rules need not apply—e.g., there is no overt top-down input to ACC. In addition, broader filter characteristics were predicted to powerfully reduce competition and increase synchrony when comparing a discrete input frequency with noise alone. This may be seen as a negative property, allowing ACC to generate associations where there are none [e.g. when they are "cognitively false" (Straube et al., 2011)]. However, it may also underlie the observed role of ACC in the formation of novel intuitive associations (Jung-Beeman et al., 2004; Mai et al., 2004).

Conclusions

A dynamic approach to understanding functional brain connectivity has previously shown that information held in neuronal oscillations can be selected and routed through the cortex on the basis of frequency- and phase-related competition. Here we present an additional dynamic process whereby different frequencies of oscillation can be combined together. The phenomenon is facilitated by the interplay between the kinetics of fast synaptic inhibition (which sets the center frequency for a given oscillation band) and the degree of heterogeneity in intrinsic electrophysiological properties of principal cells (which sets the bandwidth). Although this study has focused on ACC, it is possible that similar mechanisms could be used in other hub regions, where diverse inputs are integrated. A synergistic interplay between synaptic inhibition and intrinsic electrophysiology would provide a rich functional network structure that would be highly labile to neuromodulatory substances such as acetylcholine, dopamine, and noradrenaline (Carr et al., 2007; Hasselmo and Sarter, 2011; Gee et al., 2012; Dembrow and Johnston, 2014). We suggest that neuromodulators may modulate the degree of hub-like or input-selective functionality of higher brain structures to influence cognitive functions (Deco and Rolls, 2003).

References

Ainsworth M, Lee S, Cunningham MO, Roopun AK, Traub RD, Kopell NJ, Whittington MA (2011) Dual gamma rhythm generators control interlaminar synchrony in auditory cortex. J Neurosci 31:17040–17051. CrossRef Medline

Ainsworth M, Lee S, Cunningham MO, Traub RD, Kopell NJ, Whittington MA (2012) Rates and rhythms: a synergistic view of frequency and temporal coding in neuronal networks. Neuron 75:572–583. CrossRef Medline

Akam T, Kullmann DM (2010) Oscillations and filtering networks support flexible routing of information. Neuron 67:308–320. CrossRef Medline

Akam T, Kullmann DM (2014) Oscillatory multiplexing of population codes for selective communication in the mammalian brain. Nat Rev Neurosci 15:111–122. CrossRef Medline

Anver H, Ward PD, Magony A, Vreugdenhil M (2011) NMDA receptor hypofunction phase couples independent gamma-oscillations in the rat visual cortex. Neuropsychopharmacology 36:519–528. CrossRef Medline

Ardid S, Vinck M, Kaping D, Marquez S, Everling S, Womelsdorf T (2015) Mapping of functionally characterized cell classes onto canonical circuit operations in primate prefrontal cortex. J Neurosci 35:2975–2991. CrossRef Medline

Bassett DS, Bullmore E, Verchinski BA, Mattay VS, Weinberger DR, Meyer-Lindenberg A (2008) Hierarchical organization of human cortical networks in health and schizophrenia. J Neurosci 28:9239–9248. CrossRef Medline

Bastos AM, Usrey WM, Adams RA, Mangun GR, Fries P, Friston KJ (2012) Canonical microcircuits for predictive coding. Neuron 76:695–711. CrossRef Medline

Bastos AM, Vezoli J, Bosman CA, Schoffelen JM, Oostenveld R, Dowdall JR, De Weerd P, Kennedy H, Fries P (2015) Visual areas exert feedforward and feedback influences through distinct frequency channels. Neuron 85:390–401. CrossRef Medline

Brincat SL, Miller EK (2015) Frequency-specific hippocampal-prefrontal interactions during associative learning. Nat Neurosci 18:576–581. CrossRef Medline

Buschman TJ, Denovellis EL, Diogo C, Bullock D, Miller EK (2012) Synchronous oscillatory neural ensembles for rules in the prefrontal cortex. Neuron 76:838–846. CrossRef Medline

Cannon J, McCarthy MM, Lee S, Lee J, Börgers C, Whittington MA, Kopell N (2014) Neurosystems: brain rhythms and cognitive processing. Eur J Neurosci 39:705–719. CrossRef Medline

Carr DB, Andrews GD, Glen WB, Lavin A (2007) alpha2-Noradrenergic receptors activation enhances excitability and synaptic integration in rat prefrontal cortex pyramidal neurons via inhibition of HCN currents. J Physiol 584:437–450. CrossRef Medline

Davies DL, Bouldin DW (1979) A cluster separation measure. IEEE Trans Pattern Anal Mach Intell 1:224–227. Medline

Deco G, Rolls ET (2003) Attention and working memory: a dynamical model of neuronal activity in the prefrontal cortex. Eur J Neurosci 18:2374–2390. Medline

Dembrow NC, Chitwood RA, Johnston D (2010) Projection-specific neuromodulation of medial prefrontal cortex neurons. J Neurosci 30:16922–16937. CrossRef Medline

Dembrow N, Johnston D (2014) Subcircuit-specific neuromodulation in the prefrontal cortex. Front Neural Circuits 8:54. CrossRef Medline

Donner TH, Siegel M (2011) A framework for local cortical oscillation patterns. Trends Cogn Sci 15:191–199. CrossRef Medline

Durstewitz D, Seamans JK (2002) The computational role of dopamine D1 receptors in working memory. Neural Netw 15:561–572. Medline

Durstewitz D, Vittoz NM, Floresco SB, Seamans JK (2010) Abrupt transitions between prefrontal neural ensemble states accompany behavioral transitions during rule learning. Neuron 66:438–448. CrossRef Medline

Ferrante M, Tahvildari B, Duque A, Hadzipasic M, Salkoff D, Zagha EW, Hasselmo ME, McCormick DA (2016) Distinct functional groups emerge from the intrinsic properties of molecularly identified entorhinal interneurons and principal cells. Cereb Cortex Advance online publication. Retrieved February 8, 2017. CrossRef

Fisahn A, Pike FG, Buhl EH, Paulsen O (1998) Cholinergic induction of network oscillations at 40 Hz in the hippocampus in vitro. Nature 394:186–189. CrossRef Medline

Fisahn A (2005) Kainate receptors and rhythmic activity in neuronal networks: hippocampal gamma oscillations as a tool. J Physiol 562:65–72. CrossRef Medline

Fries P (2005) A mechanism for cognitive dynamics: neuronal communication through neuronal coherence. Trends Cogn Sci 9:474–480. CrossRef Medline

Gabbott PL, Warner TA, Jays PR, Salway P, Busby SJ (2005) Prefrontal cortex in the rat: projections to subcortical autonomic, motor, and limbic centers. J Comp Neur 492:145–177. CrossRef Medline

Gee S, Ellwood I, Patel T, Luongo F, Deisseroth K, Sohal VS (2012) Synaptic activity unmasks dopamine D2 receptor modulation of a specific class of layer V pyramidal neurons in prefrontal cortex. J Neurosci 32:4959–4971. CrossRef

Glykos V, Whittington MA, LeBeau FE (2015) Subregional differences in the generation of fast network oscillations in the rat medial prefrontal cortex (mPFC) in vitro. J Physiol 593:3597–3615. CrossRef Medline

Hájos N, Katona I, Naiem SS, MacKie K, Ledent C, Mody I, Freund TF (2000) Cannabinoids inhibit hippocampal GABAergic transmission and network oscillations. Eur J Neurosci 12:3239–3249. Medline

Hasselmo ME, Sarter M (2011) Modes and models of forebrain cholinergic neuromodulation of cognition. Neuropsychopharmacology 36:52–73. CrossRef Medline

He C, Chen F, Li B, Hu Z (2014) Neurophysiology of HCN channels: from cellular functions to multiple regulations. Prog Neurobiol 112:1–23. CrossRef Medline

Herrmann CS, Fründ I, Lenz D (2010) Human gamma-band activity: a review on cognitive and behavioral correlates and network models. Neurosci Biobehav Rev 34:981–992. CrossRef Medline

Hillman KL, Bilkey DK (2010) Neurons in the rat anterior cingulate cortex dynamically encode cost-benefit in a spatial decision-making task. J Neurosci 30:7705–7713. CrossRef Medline

Hoover WB, Vertes RP (2007) Anatomical analysis of afferent projections to the medial prefrontal cortex in the rat. Brain Struct Funct 212:149–179. CrossRef Medline

Hormuzdi SG, Pais I, LeBeau FE, Towers SK, Rozov A, Buhl EH, Whittington MA, Monyer H (2001) Impaired electrical signaling disrupts gamma frequency oscillations in connexin 36-deficient mice. Neuron 31:487–495. Medline

Hutcheon B, Yarom Y (2000) Resonance, oscillation and the intrinsic frequency preferences of neurons. Trends Neurosci 23:216–222. Medline

Hyman JM, Whitman J, Emberly E, Woodward TS, Seamans JK (2013) Action and outcome activity state patterns in the anterior cingulate cortex. Cereb Cortex 23:1257–1268. CrossRef Medline

Ito S, Stuphorn V, Brown JW, Schall JD (2003) Performance monitoring by the anterior cingulate cortex during saccade countermanding. Science 302:120–122. CrossRef Medline

Jung-Beeman M, Bowden EM, Haberman J, Frymiare JL, Arambel-Liu S, Greenblatt R, Reber PJ, Kounios J (2004) Neural activity when people solve verbal problems with insight. PLoS Biol 2:E97. CrossRef Medline

Keshavarzi S, Sullivan RK, Ianno DJ, Sah P (2014) Functional properties and projections of neurons in the medial amygdala. J Neurosci 34:8699–8715. CrossRef Medline

Kesner RP, Churchwell JC (2011) An analysis of rat prefrontal cortex in mediating executive function. Neurobiol Learn Mem 96:417–431. CrossRef Medline

Kopell N, Kramer MA, Malerba P, Whittington MA (2010) Are different rhythms good for different functions? Front Hum Neurosci 4:187. CrossRef Medline

Kopell NJ, Gritton HJ, Whittington MA, Kramer MA (2014) Beyond the connectome: the dynome. Neuron 83:1319–1328. CrossRef Medline

Kvitsiani D, Ranade S, Hangya B, Taniguchi H, Huang JZ, Kepecs A (2013) Distinct behavioral and network correlates of two interneuron types in prefrontal cortex. Nature 498:363–366. CrossRef Medline

Lakatos P, Shah AS, Knuth KH, Ulbert I, Karmos G, Schroeder CE (2005) An oscillatory hierarchy controlling neuronal excitability and stimulus processing in the auditory cortex. J Neurophysiol 94:1904–1911. CrossRef Medline

Lapish CC, Durstewitz D, Chandler LJ, Seamans JK (2008) Successful choice behavior is associated with distinct and coherent network states in anterior cingulate cortex. Proc Natl Acad Sci U S A 105:11963–11968. CrossRef Medline

Lee AT, Gee SM, Vogt D, Patel T, Rubenstein JL, Sohal VS (2014) Pyramidal neurons in prefrontal cortex receive subtype-specific forms of excitation and inhibition. Neuron 81:61–68. CrossRef Medline

Ma L, Hyman JM, Lindsay AJ, Phillips AG, Seamans JK (2014) Differences in the emergent coding properties of cortical and striatal ensembles. Nat Neurosci 17:1100–1106. CrossRef Medline

Mai XQ, Luo J, Wu JH, Luo YJ (2004) "Aha!" effects in a guessing riddle task: an event-related potential study. Hum Brain Mapp 22:261–270.

Markram H, et al. (2015) Reconstruction and simulation of neocortical microcircuitry. Cell 163:456–492. CrossRef Medline

Maulik U, Bandyopadhyay S (2002) Performance evaluation of some clustering algorithms and validity indices. IEEE Trans Pattern Anal Mach Intell 24:1650–1654. CrossRef

Middleton S, Jalics J, Kispersky T, Lebeau FE, Roopun AK, Kopell NJ, Whittington MA, Cunningham MO (2008) NMDA receptor-dependent switching between different gamma rhythm-generating microcircuits in entorhinal cortex. Proc Natl Acad Sci U S A 105:18572–18577. CrossRef Medline

Narayanan NS, Cavanagh JF, Frank MJ, Laubach M (2013) Common medial frontal mechanisms of adaptive control in humans and rodents. Nat Neurosci 16:1888–1895. CrossRef Medline

Newman LA, Creer DJ, McGaughy JA (2014) Cognitive control and the anterior cingulate cortex: how conflicting stimuli affect attentional control in the rat. J Physiol Paris 109:95–103.

Orekhova EV, Butorina AV, Sysoeva OV, Prokofyev AO, Nikolaeva AY, Stroganova TA (2015) Frequency of gamma oscillations in humans is modulated by velocity of visual motion. J Neurophysiol 114:244–255. CrossRef

Papoutsi A, Sidiropoulou K, Cutsuridis V, Poirazi P (2013) Induction and modulation of persistent activity in a layer V PFC microcircuit model. Front Neural Circuits 7:161. CrossRef

Park HJ, Friston K (2013) Structural and functional brain networks: from connections to cognition. Science 342:1238411. CrossRef Medline

Perry G, Randle JM, Koelewijn L, Routley BC, Singh KD (2015) Linear tuning of gamma amplitude and frequency to luminance contrast: evidence from a continuous mapping paradigm. PLoS One 10:e0124798. CrossRef Medline

Phillips WA, von der Malsberg C, Singer W. (2010) Dynamic coordination in the brain. In: Von der Malsberg C, Phillips WA, Singer W (eds). Dynamic Coordination in the Brain. MIT Press, Cambridge, MA.

Pinto L, Dan Y (2015) Cell-type-specific activity in prefrontal cortex during goal-directed behavior. Neuron 87:437–450. CrossRef Medline

Roopun AK, Kramer MA, Carracedo LM, Kaiser M, Davies CH, Traub RD, Kopell NJ, Whittington MA (2008a) Temporal interactions between cortical rhythms. Front Neurosci 2:145–154.

Roopun AK, Kramer MA, Carracedo LM, Kaiser M, Davies CH, Traub RD, Kopell NJ, Whittington MA (2008b) Period concatenation underlies interactions between gamma and beta rhythms in neocortex. Front Cell Neurosci 2:1.

Roopun AK, Middleton SJ, Cunningham MO, LeBeau FE, Bibbig A, Whittington MA, Traub RD (2006) A beta2-frequency (20-30 Hz) oscillation in nonsynaptic networks of somatosensory cortex. Proc Natl Acad Sci U S A 103:15646–15650. CrossRef Medline

Shenhav A, Botvinick MM, Cohen JD (2013) The expected value of control: an integrative theory of anterior cingulate cortex function. Neuron 79:217–240. CrossRef Medline

Sosulina L, Meis S, Seifert G, Steinhäuser C, Pape HC (2006) Classification of projection neurons and interneurons in the rat lateral amygdala based upon cluster analysis. Mol Cell Neurosci 33:57–67. CrossRef Medline

Steullet P, Cabungcal JH, Cuénod M, Do KQ (2014) Fast oscillatory activity in the anterior cingulate cortex: dopaminergic modulation and effect of perineuronal net loss. Front Cell Neurosci 8:244 CrossRef Medline

Straube B, Green A, Chatterjee A, Kircher T (2011) Encoding social interactions: the neural correlates of true and false memories. J Cogn Neurosci 23:306–324. CrossRef Medline

Teixeira CM, Pomedli SR, Maei HR, Kee N, Frankland PW (2006) Involvement of the anterior cingulate cortex in the expression of remote spatial memory. J Neurosci 26:7555–7564. CrossRef Medline

Thomson AM, West DC, Hahn J, Deuchars J (1996) Single axon IPSPs elicited in pyramidal cells by three classes of interneurones in slices of rat neocortex. J Physiol 496:81–102. CrossRef

van Aerde KI, Feldmeyer D (2015) Morphological and physiological characterization of pyramidal neuron subtypes in rat medial prefrontal cortex. Cereb Cortex 25:788–805. CrossRef Medline

van Burik M, Knösche T, Edlinger G, Neuper C, Pfurtscheller G, Peters M (1998) Post-movement beta oscillations studied with linear estimation. Electroencephalogr Clin Neurophysiol 106:195–198. Medline

Vogt BA, Paxinos G (2014) Cytoarchitecture of mouse and rat cingulate cortex with human homologies. Brain Struct Funct 219:185–192. CrossRef Medline

Walton ME, Bannerman DM, Alterescu K, Rushworth MF (2003) Functional specialization within medial frontal cortex of the anterior cingulate for evaluating effort-related decisions. J Neurosci 23:6475–6479. Medline

Wang XJ, Buzsáki G (1996) Gamma oscillation by synaptic inhibition in a hippocampal interneuronal network model. J Neurosci 16:6402–6413. Medline

Wartman BC, Gabel J, Holahan MR (2014) Inactivation of the anterior cingulate reveals enhanced reliance on cortical networks for remote spatial memory retrieval after sequential memory processing. PLoS One 9:e108711. CrossRef Medline

Whittington MA, Cunningham MO, LeBeau FE, Racca C, Traub RD (2011) Multiple origins of the cortical gamma rhythm. Dev Neurobiol 71:92–106. CrossRef Medline

Whittington MA, Traub RD, Jefferys JG (1995) Synchronized oscillations in interneuron networks driven by metabotropic glutamate receptor activation. Nature 373:612–615. CrossRef Medline

Yamada W, Koch C, Adams P (1998). Multiple channels and calcium dynamics. In: Koch C, Segev I (eds). Methods in neuronal modelling: from ions to networks. MIT Press, Cambridge, MA.

Yang CR, Seamans JK, Gorelova N (1996) Electrophysiological and morphological properties of layers V-VI principal pyramidal cells in rat prefrontal cortex in vitro. J Neurosci 16:1904–1921. Medline